



1

2

3 **Technical note: A low-cost albedometer for snow and ice measurements –**

4 **Theoretical results and application on a tropical mountain in Bolivia**

5 Thomas Condom^{1*}, Marie Dumont², Lise Mourre¹, Jean Emmanuel Sicart¹, Antoine
6 Rabatel¹, Alessandra Viani¹, Alvaro Soruco³

7 [1] Université de Grenoble Alpes, IRD, CNRS, Grenoble-INP, IGE (UMR5001), F-
8 38000 Grenoble, France

9 [2] Météo-France, CNRS, CNRM-GAME/CEN (UMR3589), Grenoble, France

10 [3] UMSA, Instituto de Geológicas y del Medio Ambiente, La Paz, Bolivia

11

12 *Corresponding author: thomas.condom@ird.fr

13



14 **Abstract**

15 This study presents a new instrument called a low-cost albedometer (LCA) composed
16 of two illuminance sensors that are used to measure *in-situ* incident and reflected
17 illuminance values on a daily timescale. The ratio between reflected vs. incident
18 illuminances is called the *albedo index* and can be compared with actual albedo values.
19 Due to the shape of the sensor, the direct radiation for zenith angles ranging from 55°
20 to 90° is not measured. The spectral response of the LCA varies with the solar
21 irradiance wavelengths within the range 0.26 to 1.195 μm, and the LCA detects 85%
22 of the total spectral solar irradiance for clear sky conditions. We first consider the
23 theoretical results obtained for 10 different ice and snow surfaces with clear sky and
24 cloudy sky incident solar irradiance that show that the LCA spectral response may be
25 responsible for an overestimation of the theoretical albedo values by roughly 9% at
26 most. Then, the LCA values are compared with two “classical” albedometers over a
27 one-year measurement period (2013) for two sites in a tropical mountainous catchment
28 in Bolivia. One site is located on the Zongo Glacier (i.e. snow and ice surfaces) and
29 the second one is found on the right-hand side lateral moraine (bare soil and snow
30 surfaces). The results, at daily time steps (256 days), given by the LCA are in good
31 agreement with the classic albedo measurements taken with pyranometers with $R^2 =$
32 0.83 (RMSD = 0.10) and $R^2 = 0.92$ (RMSD = 0.08) for the Zongo Glacier and the right-
33 hand side lateral moraine, respectively. This demonstrates that our system performs
34 well and thus provides relevant opportunities to document spatio-temporal changes in
35 the surface albedo from direct observations at the scale of an entire catchment at a
36 low cost. Finally, during the period from September 2015 to June 2016, direct
37 observations were collected with 15 LCAs on the Zongo Glacier and successfully
38 compared with LANDSAT images showing the surface state of the glacier (i.e. snow



39 or ice). This comparison illustrates the efficiency of this system to monitor the daily
40 time step changes in the snow/ice coverage distributed on the glacier.

41 **Keywords:** Snow; Ice; Albedo; Glacier, Bolivia

42 **1-Introduction**

43 Albedo is a key variable controlling the surface energy balance through the shortwave
44 radiation budget. Documenting the spatio-temporal changes of this variable is a major
45 concern in hydrological modeling particularly in mountainous regions where the
46 seasonal snow and glacier covers induce significant and rapid changes in the surface
47 state with subsequent impacts on the energy budget. Hereafter, the spectral albedo is
48 defined as the ratio between the amount of energy reflected by the surface and the
49 incident energy for each wavelength of the solar spectrum (between 0.3 and 2.5 μm);
50 and the broadband albedo is the integration of the spectral albedo weighted by the
51 incident energy over the entire solar spectrum (0.3-2.5 μm). The amount of shortwave
52 radiation absorbed by the surface depends on the spectral and angular distribution of
53 the incident shortwave radiation and the surface characteristics, both of which are
54 highly variable in space and time (Stroeve *et al.*, 1997; Klok *et al.*, 2003). Clouds alter
55 the angular and spectral properties of the incident radiation. With respect to the snow
56 and ice surfaces, the albedo in the visible wavelength depends on the snow and ice
57 properties, the impurity amount (e.g. black carbon, dust, algae, etc.) and the snow
58 depth for the shallow snowpack. In the infrared portion of the spectrum, the albedo is
59 mainly controlled by the snow microstructure and is moderately sensitive to the solar
60 zenith angle (Warren, 1982). Liquid water and land have relatively low albedos (roughly
61 0.1 to 0.4) while snow and ice have higher albedos that typically can reach 0.9 for fresh
62 snow. It is still challenging to measure the temporal and spatial changes in the surface



63 albedo from the scale of specific points up to a regional scale. Different methods are
64 commonly used to retrieve albedo values from satellite images, ground photographs
65 or point measurements with pyranometers. Satellite-derived albedo maps provide
66 spatially continuous datasets but are limited to clear sky conditions; these maps may
67 contain significant uncertainties, especially over complex topographies (Stroeve *et al.*,
68 1997; Klok *et al.*, 2003; Dumont *et al.*, 2012), and provide averaged data over a pixel
69 size of hundreds of square meters. Ground photography using pairs of photographs in
70 the visible and infrared wavelengths is used to collect albedo maps that have a higher
71 spatial resolution than satellite images but which are limited by cloudy conditions, the
72 possible masking of the relief, an irregular grid due to the projection and more complex
73 ortho-rectification processes in mountainous regions (e.g. Corripio, 2004; Dumont *et al.*,
74 2011). Finally, direct *in situ* snow and ice albedo measurements are sparse,
75 relatively expensive, often discontinuous and may contain large uncertainties if the
76 sensor is not regularly checked (Sicart *et al.*, 2001, van den Broeke *et al.*, 2004).

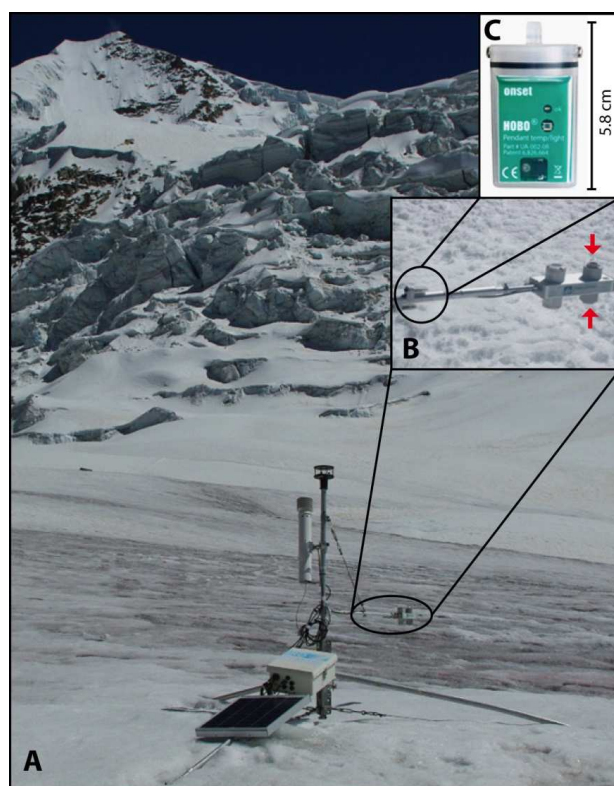
77 This article analyzes the efficiency of a low-cost albedometer (hereafter called LCA)
78 that measures the time series of *in-situ* incident and reflected illuminance values which
79 are used to calculate an accurate proxy of the albedo values called the *albedo index*.
80 The illuminance is the total luminous flux incident on a surface, per unit area. It is a
81 measure of how much the incident light illuminates the surface, wavelength-weighted
82 by the luminosity function to correlate with the human perception of brightness. In
83 section 2, we present the characteristics of and uncertainties on the LCA
84 measurements along with a comparison with the theoretical values for 10 different ice
85 and snow states and for two different incident irradiance spectra (cloudy or clear sky).
86 Then, section 3 presents two experiments carried out on a high-altitude tropical
87 mountain site in Bolivia (Zongo glacierized catchment). A first application for punctual



88 *in situ* measurements validates the LCA in the field via a comparison with classical
89 radiometers for two contrasting surfaces: snow/ice on the glacier or snow/bare soil on
90 the moraine. After that, a second application on the same glacier documents the
91 snow/ice changes on the surface of the glacier during the period that extends from
92 September 2015 to June 2016.

93 **2- LCA description and evaluation with theoretical albedo values for snow and**
94 **ice surfaces**

95 The LCA is comprised of two Hobo® Pendant Temperature/Light Data Loggers: one
96 for the incident illuminance and the other for the reflected illuminance (Fig. 1). The
97 sensor characteristics are given in Table 1. This sensor measures the illuminance in
98 lux and the measurement range is between 0 and 320,000 lux. The lux quantifies the
99 light incident flux per unit area. One lux equals one lumen per square meter with a
100 uniform distribution. In photometry, this unit is used as a measure of the intensity of
101 the light hitting or passing through a surface as perceived by the human eye. The
102 illuminance may be related to an energy quantified in watts per square meter (W/m^2),
103 but the conversion factor differs depending on the wavelength considered according to
104 the luminosity function, a standardized model of the human visual perception of
105 brightness. As a consequence, the illuminance depends on the spectral distribution of
106 the incident light.



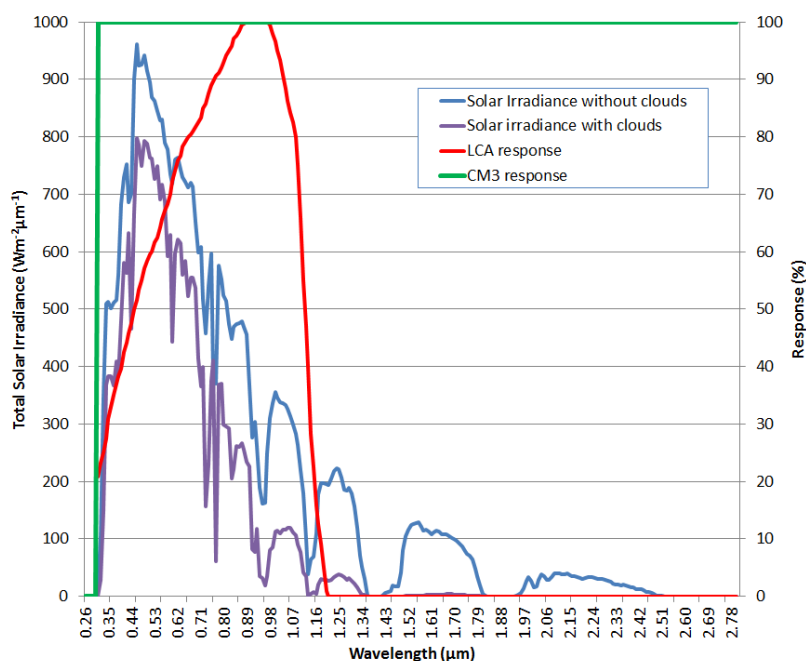
107

108 **Figure 1:** A) Meteorological station on the Zongo Glacier; B) CNR1 radiometer (Kipp & Zonen) installed
109 at the SAMA meteorological station (the CM3 pyranometers are the two sensors on the right, red arrows)
110 and the LCA comprised of two Hobo® Pendant Temperature/Light Data Loggers (black arrows); C) Zoom
111 on a Hobo® Pendant Temperature/Light Data Logger (see Table 1 for detailed characteristics).

112 The spectral range of the Hobo® Pendant Temperature/Light Data Logger is 0.3 to
113 1.195 μm (see Fig. 2). The spectral response of the sensor represents the amount of
114 incoming signal recorded by the sensor for any given wavelength and is reported in
115 Figure 2. Figure 2 shows that the spectral response of the sensor increases from 20 to
116 100% between 0.26 and 0.915 μm and then decreases until the upper limit of the
117 sensor sensitivity (i.e. 1.195 μm). The sensor detects roughly 85% of the total solar
118 irradiance for clear sky conditions (Fig. 2). Laboratory tests conducted with a
119 goniometer showed that the Hobo® Pendant Temperature/Light Data Logger cannot



120 measure the irradiance for incident zenith angles ranging from 55° to 90° (+/- 2°, where
121 0° is the vertical illumination). This is due to the design of the sensor (Fig. 1C).
122 Traditionally, the *in situ* albedo is measured using a CM3 pyranometer (Kipp & Zonen®)
123 in the shortwave domain from 0.305 to 2.800 μm (Fig. 1B). The CM3 is part of the
124 CNR1/CNR4 net radiometer, which is intended for the analysis of the radiation balance
125 of solar and thermal infrared radiation. The design of the CM3 is such that the upward-
126 facing and downward-facing sensors measure the energy received from the entire
127 hemisphere (a field of view of almost 180 degrees). The output is expressed in W/m².
128 The CM3 sensor has a 100% response for wavelengths between 0.305 to 2.8 μm (Fig.
129 2).





131 **Figure 2:** *Hobo® Pendant Temperature/Light Data Logger and CM3 responses as a function of*
132 *the wavelength and two examples of total solar irradiances for a clear sky in blue and for a cloudy sky*
133 *in purple given by the DISORT model (Stamnes et al., 1988) ($Wm^2\mu m^{-1}$)*

134 **Table 1:** *Characteristics of the Hobo® Pendant Temperature/Light Data Logger sensor as per*
135 *the manufacturer*

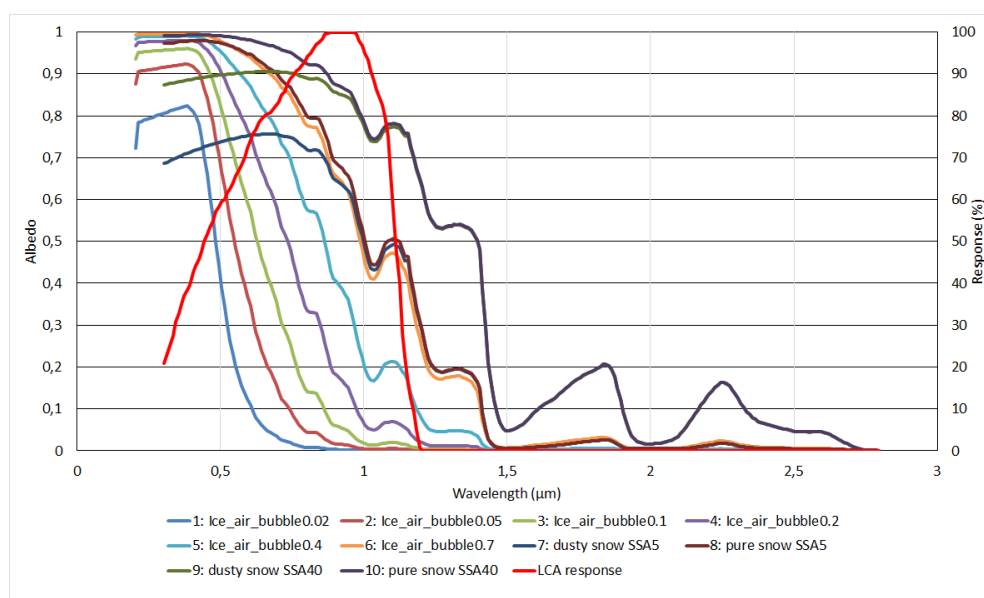
| | |
|-----------------|---|
| Measurement | Temperature: -20° to 70°C |
| Range | Light: 0 to 320,000 lux |
| Accuracy | Temperature: +/- 0.53°C Light intensity designed for measurement of relative light levels, see Figure 2 for the light wavelength response |
| Resolution | Temperature: 0.14°C at 25°C |
| Time accuracy | +/- 1 minute per month at 25°C |
| Operating range | in air: -20° to 70°C |
| Battery life | 1 year typical use |
| Memory | 64 K bytes |
| Material | Polypropylene case; stainless steel screws; Buna-N o-ring |
| Weight | 18 g |
| Dimensions | 58 x 33 x 23 mm |

136

137 It is noteworthy that the LCA contains an internal memory; this is not the case for the
138 CM3 pyranometers, which need to be connected to an external module for data
139 acquisition programming and data storage. The LCA cannot provide direct access to
140 the albedo as its response is not constant depending on the wavelength in the solar
141 spectrum. Finally, the conversion from illuminance to radiation in W/m^2 is not
142 straightforward since it depends on the spectral repartition of the incident and reflected
143 light.



144



145

146 **Figure 3:** Semi-infinite diffuse beam albedo of pure ice as a function of the effective air bubble radius
147 (mm) with a constant effective bubble concentration $n'_b = 0.3 \text{ mm}^{-3}$. Here 0.3 mm^{-3} is the mean bubble
148 concentration determined from 28 Greenland and Antarctica ice core samples (Gardner and Sharp,
149 2010) - Semi-infinite diffuse beam albedo of dusty and pure snow from DISORT modelling with or without
150 dust and with a specific surface area (SSA) equal to 40 or $5 \text{ m}^2 \text{ kg}^{-1}$ [Stamnes et al., 1988; Carmagnola
151 et al., 2013]. The dark green line shows the LCA response in %.

152 Figure 3 shows 10 simulated spectral albedo curves for different glacier surfaces, four
153 for snow (with dusty or pure snow and with a specific surface area (SSA) equal to 5 or
154 $40 \text{ m}^2 \text{ kg}^{-1}$) and six for ice with different bubble concentrations (see Gardner and Sharp,
155 2010 for details). These 10 different surface types are used below to calculate the
156 theoretical uncertainty of the LCA measurements.

157 In the visible domain, the spectral albedo of pure snow is high (0.95) and the albedo
158 decreases in the infrared towards 0.1 for larger wavelengths (1.5-2 μm) (Fig. 3). For
159 dusty snow, the spectral albedo is lower than for pure snow. To calculate the



160 uncertainty for the ice covers, we chose pure ice that only contains air bubbles and no
161 impurity taken from the study of Gardner and Sharp (2010). In this case, all of the
162 photon absorption events will occur within the ice and all of the scattering will occur at
163 the ice-bubble boundaries, thereby neglecting all surface reflection as well as internal
164 scattering and absorption by the interstitial air (Mullen and Warren, 1988; Warren *et*
165 *al.*, 2002).

166 Two types of incident radiations are tested (clear sky and cloudy conditions given by
167 the SBDART model for the tropical Zongo latitude at 5000 m a.s.l., 23° solar zenith
168 angle, 0.1 atmospheric optical depth, (see Richiazzi *et al.*, 1998 for details
169 concerning the model). The cloudy conditions are fully overcast with a cloud optical
170 depth equal to 64.

171 The theoretical broadband albedo and LCA *albedo indexes* are calculated over the
172 0.205-3.9 μm range using the theoretical solar irradiance and LCA spectral response
173 from Figure 2 and the semi-infinite diffuse beam albedo from Figure 3. The total
174 incident radiation flux for LCA is obtained by summing the theoretical incident radiation
175 fluxes weighted by the LCA response at each spectral increment of 5 microns, both for
176 cloudy and clear sky conditions. Similarly, the reflected radiation flux for the LCA is
177 obtained by summing the theoretical reflected radiation fluxes weighted by the LCA
178 response at each spectral increment of 5 μm , for each snow or ice class considered.
179 Then, the LCA *albedo index* is the ratio between the reflected and incident LCA
180 radiation fluxes, for each type of snow and ice surface and for cloudy or clear sky
181 conditions. Finally, this LCA *albedo index* is compared with the theoretical broadband
182 albedo when we consider the spectral variations. Note that the results are presented
183 with the incoming radiation corresponding to the total solar irradiances for clear sky



184 and cloudy sky conditions and without testing the effect of the angular limitation of the
185 LCA.

186

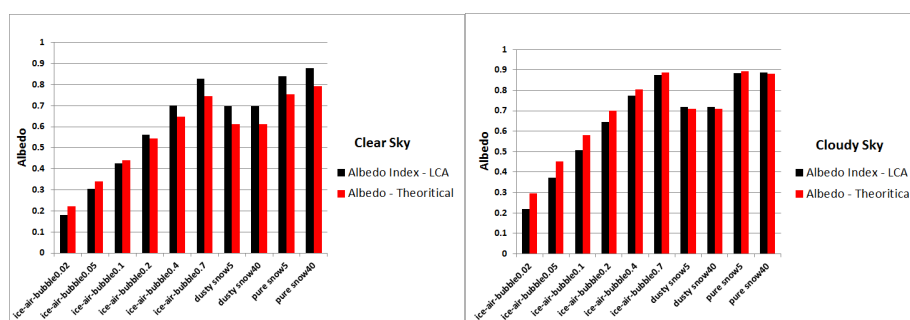
187

188

189

190

191



192 **Figure 4:** Comparison between the theoretical semi-infinite diffuse beam broadband albedo
193 and albedo index calculated with the LCA for 10 different surfaces calculated with two kind of total solar
194 irradiance; on the right: cloudy sky and on the left: clear sky conditions (spectra are represented in Fig.
195 2) - 1: Ice air bubble 0.02; 2: Ice air bubble 0.05; 3: Ice air bubble 0.1; 4: Ice air bubble 0.2; 5: Ice air
196 bubble 0.4; 6: Ice air bubble 0.7; 7: dusty snow SSA $5 \text{ m}^2 \text{ kg}^{-1}$; 8: dusty snow SSA $40 \text{ m}^2 \text{ kg}^{-1}$; 9: pure
197 snow SSA $5 \text{ m}^2 \text{ kg}^{-1}$; 10: pure snow SSA $40 \text{ m}^2 \text{ kg}^{-1}$

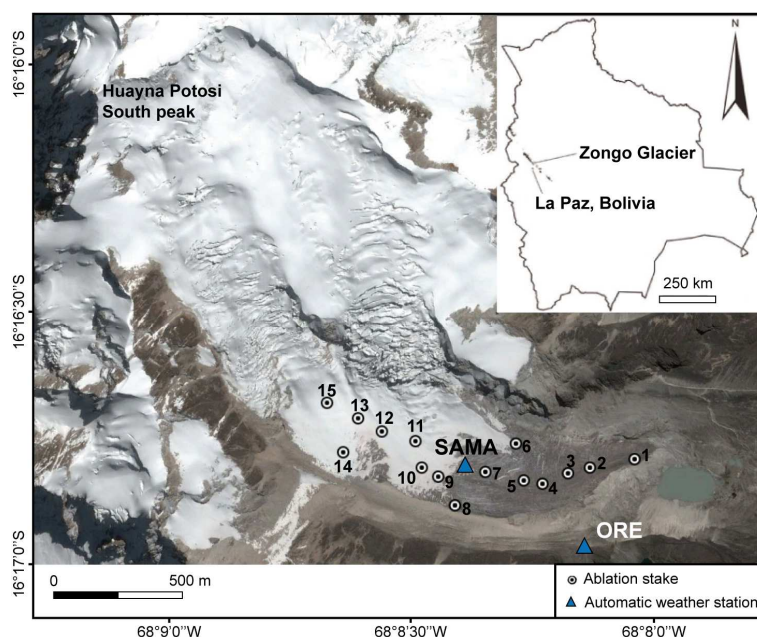
198 Figure 4 compares the theoretical albedos and the LCA *albedo index* with the
199 theoretical perfect albedo for the 10 surface configurations and for clear and cloudy
200 skies. Slight differences exist for ice with a bubble radius between 0.02 and 0.2 mm
201 with an underestimation of the LCA by 4% for a clear sky. For ice with an air bubble



202 radius of 0.4 or 0.7 mm and for the two snow types (dusty and pure), the LCA tends to
203 overestimate the albedo by 8% in average for clear sky conditions. The LCA tends to
204 overestimate for albedo values higher than 0.5 (typically for snow) and to
205 underestimate for low values (i.e. for ice). A better agreement between the two sensors
206 is given in the cloudy case with an overall underestimation of 5% compared with 9%
207 for the clear sky case. This is explained by the response of the LCA based on the
208 wavelength, which is null for the 1.20-2.30 μm range (see Fig. 2).

209 **3-Applications on a high tropical glacierized catchment in Bolivia**

210 The Zongo Glacier (16°15'S, 68°10'W) is located in the Bolivian Cordillera Real (Fig.
211 5) between the Altiplano Plateau in the west and the Amazon Basin in the east. In
212 2006, the glacier covered an area of 1.96 km² extending from 6100 to 4900 m a.s.l.
213 (Rabatel *et al.*, 2012). The Bolivian Cordillera Real is located in the outer tropical zone,
214 which forms a transition zone between the tropics (continuously humid conditions) and
215 the subtropics (dry conditions). The climate of the outer tropics is characterized by low
216 seasonal temperature variability, high solar radiation influx all year round and marked
217 seasonal humidity and precipitation. The hydrological year (from September 1st to
218 August 31st) can be divided into three periods: (1) September–December, with a
219 progressive increase in moisture and precipitation; (2) January–April, which is the core
220 period of the rainy season (approximately two-thirds of the total annual precipitation);
221 and (3) May–August, when dry conditions prevail (e.g. Sicart *et al.*, 2011). However,
222 precipitation can also occur during the dry period due to Southern Hemisphere mid-
223 latitude disturbances that track much further north of their usual path (e.g. Vuille and
224 Ammann, 1997; Sicart *et al.*, 2016).



225

226 **Figure 5:** Study site with the Zongo Glacier and the location of the meteorological stations: ORE (5050
227 m a.s.l.) outside of the glacier and SAMA (5056 m a.s.l.) on the glacier. The numbers indicate the
228 position of each *in situ* LCA on ablation stakes.

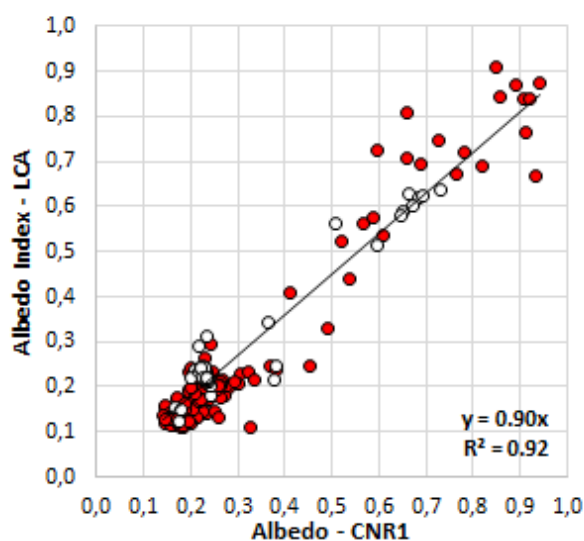
229 Two contrasting sites with different characteristics were chosen in order to evaluate
230 the efficiency of the LCA (Figure 5). These two sites belong to the GLACIOCLIM
231 observatory (<https://glacioclim.osug.fr/>) which has maintained a permanent glacio-
232 meteo-hydrological monitoring program on the Zongo Glacier since 1991 (Rabatel *et*
233 *al.*, 2013). The SAMA station is an automatic weather station (AWS) located on the
234 Zongo Glacier (Figures. 1, 5) and the ORE station is a similar AWS located on the
235 right-hand side lateral moraine. In order to capture the sky view for each station, ORE
236 and SAMA, a digital elevation model (DEM) at 30-m resolution taken from ASTER
237 images (Tachikawa *et al.*, 2011) was used. The sky view factor, which is the fraction
238 of the celestial hemisphere visible from the surface defined by the local slope, was
239 calculated with the SAGA GIS software (System for Automated Geoscientific Analyses,



240 version 2.0.8) using the code provided by Boehner and Antonic (2009). The sky view
241 factors obtained are 0.92 and 0.98 for the SAMA and ORE stations, respectively.

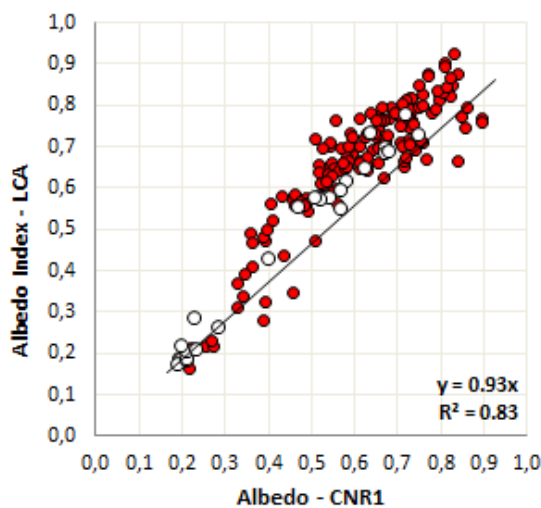
242 Considering the limited field of view of the Hobo® Pendant Temperature/Light
243 Data Logger, daily albedo values are calculated between 11:00 AM and 3:00 PM local
244 time, ensuring that direct solar irradiance is caught by the two sensors. The *albedo*
245 *index* is calculated in two steps: (i) the sum of the hourly data for the incident
246 illuminance and the reflected illuminance between 11:00 AM and 3:00 PM; and (ii) the
247 calculation of the daily *albedo index* by dividing the reflected values by the incident
248 illuminance values. The time series used for the ORE and SAMA stations are
249 07/11/2012-06/03/2013 and 01/12/2012- 9/10/2013 respectively. Figures 6A and 6B
250 show the comparison between the CM3 albedo and LCA *albedo indexes* for the daily
251 values that range between 0.15 (dirty ice or bare soil) and 0.95 (fresh snow).

252



253

A



254

B

255 **Figure 6:** **A** Comparison of the daily measured albedo at the ORE site using the CNR1
256 radiometer and the LCA for the period from 07/11/2012–06/03/2013– daily data calculated for the 11 AM
257 – 3 PM time period – ORE; RMSD = 0.1; n = 263. **B** Comparison of the daily measured albedo at the
258 SAMA site on the Zongo Glacier using the CM3 sensor and LCA for the period from 01/12/2012–
259 9/10/2013 – daily data calculated for the 11 AM – 3 PM time period; RMSD = 0.08; n = 256. The red
260 dots are for cloudy conditions and the white dots are for sunny conditions, as per the classification given
261 by Sicart et al. (2016). The regression lines are calculated with all of the data.

262 At the ORE site (Figure 6A), two groups of points can be distinguished. The lower
263 group (albedo close to 0.25) corresponds to measurements over bare soil. For the
264 second group, the broadband albedo and *albedo indexes* range from 0.3 to 0.9,
265 corresponding to several snow cover conditions: (i) thin and dirty snow; (ii)
266 homogeneous fresh snow; and (iii) patchy snow covers. There is good agreement
267 between the CM3 broadband albedos and LCA broadband *albedo indexes* ($R^2 = 0.90$
268 and RMSD = 0.08, with 256 days). The distribution for the albedos at the SAMA site
269 (Figure 6B) is more homogeneous. For the SAMA site, the albedo variations are due
270 to surface changes from ice to fresh snow. At this second site, there is also good



271 agreement between the CM3 and LCA albedo ($R^2 = 0.93$ and $RMSD = 0.08$, with 256
272 days).

273 The measurements are separated into two groups according to the sky conditions,
274 cloudy or sunny, as per the classification provided by Sicart et al. (2016). If we consider
275 the theoretical results from section 2, the LCA should give better results for cloudy
276 conditions; however there are not enough measurements for clear sky conditions
277 compared with the number of measurements for cloudy conditions to be able to come
278 to a conclusion. In both cases, the LCA tends to slightly overestimate the albedo values
279 by 5%. This result is in good agreement with the theoretical results presented in
280 Section 2 (Figure 4) showing that the LCA tends to overestimate the theoretical albedo
281 values for ice with bubbles and snow by less than 10%. The results are in good
282 agreement with the theoretical results obtained in section 2, with an overestimation for
283 the high albedos and an underestimation for the low albedos.

284 After the comparison between the CM3 and LCA, a second field experiment was
285 carried out in order to determine the spatio-temporal variability of the snow cover on
286 the Zongo Glacier during the period from 09/21/2015 to 06/30/2016. Fifteen LCA
287 stations were installed on ablation stakes distributed in the lower and middle part of
288 the glacier at altitudes ranging between 4929 and 5184 m a.s.l. (Figure 5). In order to
289 evaluate whether the LCA provides coherent information on the spatio-temporal
290 changes in the surface state of the glacier (fresh snow, old snow, ice), we compared
291 the LCA data with information retrieved from the LANDSAT images. With regards to
292 the LANDSAT images (30-m resolution), we first selected, within the archive, the cloud
293 free images recorded within the period when the LCA data were available (a list of the
294 23 images used here is provided in Table 2). On the LANDSAT images, we used a
295 spectral band combination involving the green, near-infrared (NIR) and middle infrared



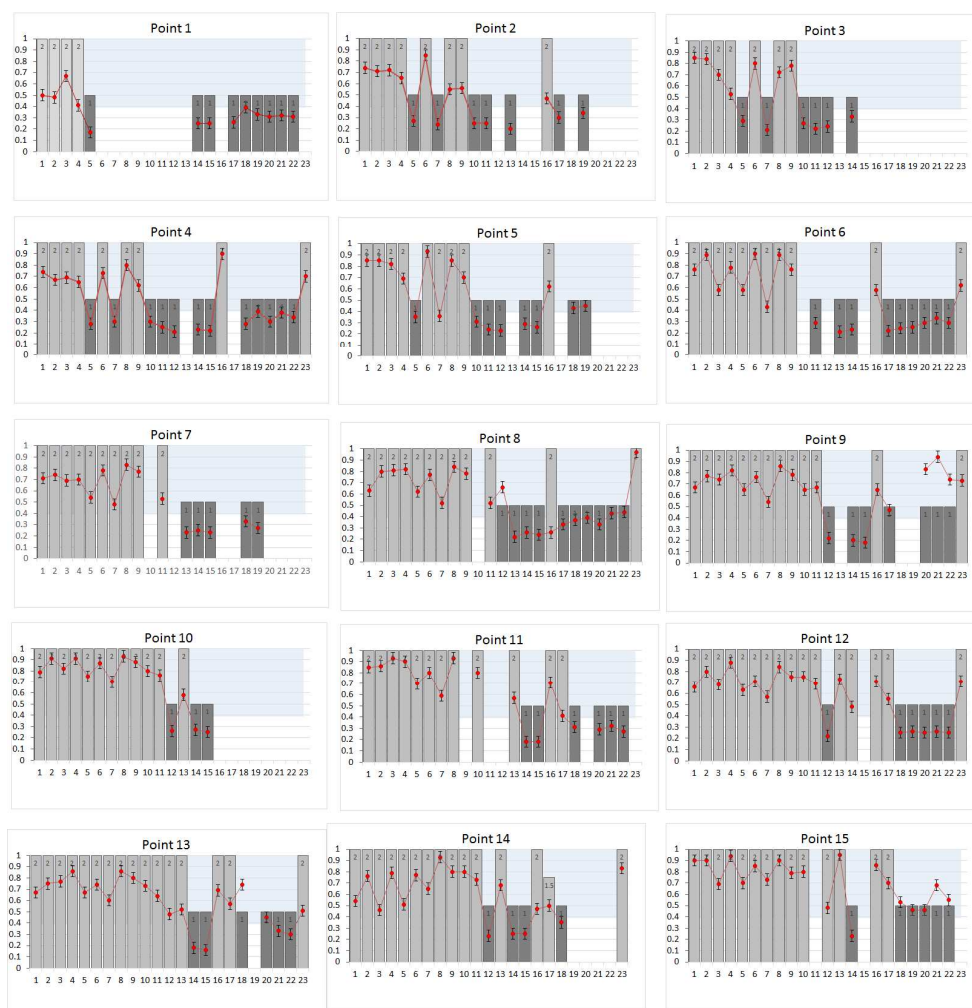
296 (MIR) wavelengths (spectral bands # 2, 4 and 5 for LANDSAT images 5 and 7) which
297 is used to make a clear differentiation between snow and ice surfaces (Rabatel *et al.*,
298 2012). Then, according to the values in the NIR and MIR bands, the pixels where the
299 LCA are located were classified as snow covered (value of 2 in Figure 7) or ice covered
300 (value of 1 in Figure 7). In one case, the chosen value was 1.5 as the pixel showed
301 patchy snow cover. This can be explained if we consider that the spatial resolution of
302 the LANDSAT is equal to 900 m² and the surface view by the sensor is less than 1 m².

303 *Table 2: Date of the LANDSAT images used in the present study (Path/Row = 001/071)*
304 *(images from the web site: <https://landsatlook.usgs.gov/viewer.html>)*

| Date of the LANDSAT images | No. |
|----------------------------|-----|
| 10/18/2015 | 1 |
| 11/03/2015 | 2 |
| 11/11/2015 | 3 |
| 11/19/2015 | 4 |
| 12/05/2015 | 5 |
| 12/13/2015 | 6 |
| 01/06/2016 | 7 |
| 01/14/2016 | 8 |
| 01/22/2016 | 9 |
| 02/15/2016 | 10 |
| 03/18/2016 | 11 |
| 03/26/2016 | 12 |
| 04/03/2016 | 13 |
| 04/11/2016 | 14 |
| 04/27/2016 | 15 |
| 05/13/2016 | 16 |
| 05/21/2016 | 17 |
| 05/29/2016 | 18 |
| 06/06/2016 | 19 |
| 06/14/2016 | 20 |
| 06/22/2016 | 21 |
| 06/30/2016 | 22 |
| 07/08/2016 | 23 |

305

306



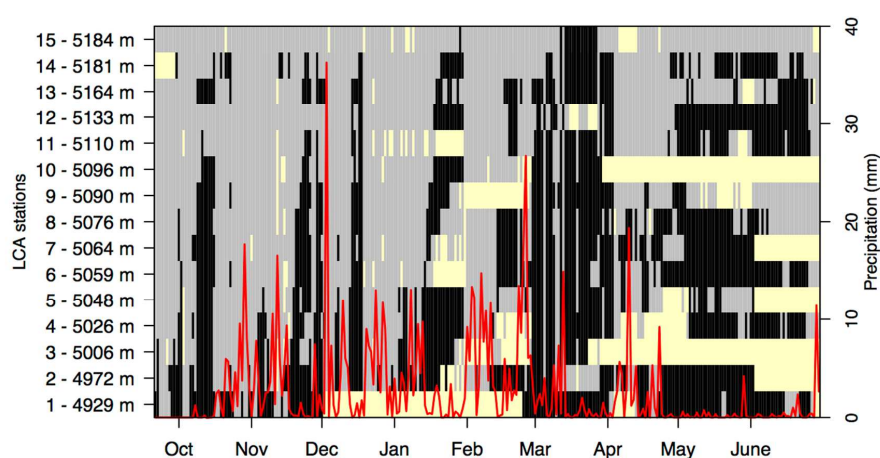
307

308 *Figure 7: Comparison between the LCA measurements and the 23 LANDSAT images (from*
 309 *10/18/2015 to 06/30/2016, the numbers for the Y axis are the image numbers, see Table 2 for the*
 310 *correspondence) for the 15 points on the Zongo Glacier (see Figure 5 for the locations of the LCA). The*
 311 *red points represent the albedo index value calculated with the LCA and the grey bars indicate the*
 312 *surface state for the corresponding pixel (1: ice and 2: snow). A value of 1.5 was chosen for stake*
 313 *number 14 as the pixel showed patchy snow cover.*

314 The LCA network was deployed in the lower and middle part of the Zongo Glacier
 315 (Figure 5) which is the zone where the snowline altitude goes up or down depending



316 on the snowfall events and ablation processes. For all of the points, we identified a first
317 period (10/18/2015 to 11/11/2015) with high albedo values comprised between 0.40
318 and 0.92. These values are in agreement with the surface state of the glacier on the
319 LANDSAT images where the pixels of the glacier tongue are all snow covered. During
320 the second period, the glacier surface is covered by ice or by snow depending on the
321 altitude. In further detail, we identified three groups organized by altitude ranges
322 depending on the changes in the surface state of the glacier with a first group in the
323 lower part of the glacier (LCA numbers 1, 2, 3, 4, 5), a second group in the middle part
324 of the glacier (LCA numbers 6, 7, 8, 9, 10, 11, 12) and a third group with LCA numbers
325 13, 14, 15 (see Figure 5 for the location). Finally, the comparisons between the *in situ*
326 LCA measurements and the surface state given by the LANDSAT images were used
327 to visually identify a threshold for the *albedo index* equal to 0.39 between snow and
328 ice. These results are in agreement with those obtained by Sicart *et al.* (2001) which
329 showed that the albedo for the Zongo Glacier ranges from 0.3 for dirty ice to 0.9 for
330 fresh snow.





332 **Figure 8:** Daily albedo index for the 15 LCA stations during the period from 09/21/2015 to
333 06/30/2016, in yellow: missing data; binary values considering the separation between ice (1: in black)
334 and snow (2: in grey) with a threshold equal to 0.39. In red, the daily precipitation amount measured by
335 the GEONOR rain gauge at the ORE station (mm/day).

336 Figure 8 gives the evolution of the albedo for the 15 points during the period
337 09/21/2015-06/30/2016 as well as the precipitation amount measured by a GEONOR
338 precipitation gauge at the ORE station (Figure 5). We can clearly identify the snowfall
339 events and see how the snow disappears thus leaving the glacier ice exposed. As a
340 result, the snowline altitude variations can be defined and vary between 4929 and 5184
341 m a.s.l. depending on the period of the year. In further detail, it can be noted that at the
342 beginning of the study period (i.e. between September and November), the snowline
343 quickly rises up and goes down due to intermittent precipitation events. Then, during
344 the rainy season (from December to March), the glacier is mostly snow-covered
345 (mainly above 5000 m a.s.l.). Finally, during the dry season (April to June), the
346 snowline rises up to 5150 m a.s.l. and the glacier tongue is mainly snow free.

347 **4- Discussion and conclusion**

348 In this study we developed, evaluated and tested a new low-cost albedometer (LCA)
349 comprised of two Hobo® Pendant Temperature/Light Data Loggers, measuring
350 downward and upward illuminances. The measurements of the field of view of the LCA
351 in the laboratory with a goniometer showed that the LCA cannot capture the radiation
352 for zenith angles ranging from 55° to 90° (+/- 2°). Using the LCA spectral response
353 (0.205 to 1.2 µm), we evaluated the simulated *albedo index* of the LCA over different
354 types of snow and ice surfaces. The results showed that the LCA *albedo indexes* are
355 within -4% to +8% of the theoretical broadband albedo values while considering that
356 cloudy or clear sky incident irradiances only account only for the spectral response of



357 the LCA and not for the angular response of the LCA with respect to the ideal response.
358 In the second part of the study, we evaluated the LCA *albedo indexes* in the field using
359 CM3 broadband albedo values at two different sites in a tropical mountain in Bolivia:
360 on the Zongo Glacier, at one station located on the glacier and another one located on
361 the moraine. Data were recorded at hourly time steps and then the albedo indices were
362 calculated on a daily timescale (from 11:00 AM to 3:00 PM). The daily *albedo indexes*
363 from the LCA are in good agreement with the broadband albedo values derived from
364 the CM3 pyranometer. By comparing the LCA albedo estimates with the CM3
365 broadband albedo over a period of approximately 260 days at the two sites, we
366 conclude that the efficiency of the *albedo indexes* given by the LCA is +/- 0.1 compared
367 with classic CNR1 sensors. Future applications are certainly possible, especially
368 considering the low cost, the autonomy of the LCA in terms of energy and the very
369 small size of the sensors. For example, the LCA could be useful to spatialize *in situ*
370 albedos in glacierized catchments: both on the glacier, where the evolution of the snow
371 cover can be monitored, and in the non-glacierized part for the evolution of the
372 seasonal snow cover and, more generally, the changes in the ground albedo due to,
373 for example, variations in the soil moisture (Gascoin *et al.*, 2009). The comparison
374 between the LCA measurements and LANDSAT images during the period extending
375 from 10/18/2015 to 06/30/2016 showed that the LCA is a powerful tool that can be
376 used to quantify the evolution of the *albedo index* and to characterize the surface state
377 of the glacier by distinguishing between fresh snow, dirty snow and ice. In order to
378 have good results for the *albedo index* calculated with the LCA, a certain degree of
379 caution is required: for example, snow particles should not stay on the sensor and the
380 sensor must be kept horizontal. This new system has demonstrated its usefulness for
381 a tropical glacier and future studies in other climatic contexts should be conducted.



382 **5- Acknowledgments**

383 This study was funded by the French *Institut de Recherche pour le Développement*
384 (IRD) through the Andean part of the French glacier observatory service, GLACIOCLIM
385 (<http://www-lgge.ujf-grenoble.fr/ServiceObs/SiteWebAndes/index.htm>), and was
386 carried out within the framework of the International Joint Laboratory GREAT-ICE, a
387 joint initiative of the IRD as well as universities and institutions in Bolivia, Peru, Ecuador
388 and Colombia. All of the contributing authors acknowledge the contribution of LABEX
389 OSUG@2020, ANR grant No. ANR-10-LABX-56. The Pléiades satellite image used
390 for Figure 1 was obtained from the CNES-ISIS FC18473 program funded by the
391 BIOTHAW project (AAP-SCEN-2011-II). The authors would like to thank everyone who
392 participated in the field campaigns: Patrick Ginot, Maxime Harter and Pierre Vincent.

393

394 **8- References**

395 Boehner, J., Antonic, O. (2009): 'Land-surface parameters specific to topo-
396 climatology'. in: Hengl, T., Reuter, H. (Eds.): 'Geomorphometry - Concepts,
397 Software, Applications'. Developments in Soil Science, Volume 33, p.195-226,
398 Elsevier

399 Carmagnola, C. M., Domine, F., Dumont, M., Wright, P., Strellis, B., Bergin, M., et al.
400 (2013). Snow spectral albedo at Summit, Greenland: comparison between in situ
401 measurements and numerical simulations using measured physical and chemical
402 properties of the snowpack. *The Cryosphere*, 7, 1139–1160.
403 <http://dx.doi.org/10.5194/tc-7-1139-2013>. Colbeck, S.C., 1983, Theory of
404 metamorphism of dry snow, *Journal of Geophysical Research-Oceans and*
405 *atmospheres*, 88(NC9), 5475-5482



- 406 Corripio, J., 2004. Snow surface albedo estimation using terrestrial photography. *Int.*
407 *J. Remote Sensing*, 24(24), 5705-5729
- 408 Dumont, M., P. Sirguey, Y. Arnaud and D. Six. 2011. Monitoring spatial and temporal
409 variations of surface albedo on Saint Sorlin Glacier (French Alps) using terrestrial
410 photography. *Cryosphere*, 5, 759-771. doi: 10.5194/tc-5-759-2011
- 411 Dumont, M., J. Gardelle, P. Sirguey, A. Guillot, D. Six, A. Rabatel and Y. Arnaud.
412 2012. Linking glacier annual mass balance and glacier albedo retrieved from MODIS
413 data. *Cryosphere*, 6, 1527-1539. doi: 10.5194/tc-6-1527-2012
- 414 Gascoin, S., Ducharne, A., Ribstein, P., Perroy, E., Wagnon, P., 2009, Sensitivity of
415 bare soil albedo to surface soil moisture on the moraine of the Zongo glacier
416 (Bolivia), *Geophysical Research Letters*, volume 36, Issue 2,
417 DOI: 10.1029/2008GL036377
- 418 Gardner, A.S., Sharp, M.J., 2010, A review of snow and ice albedo and the
419 development of a new physically based broadband albedo parameterization,
420 *Journal of Geophysical Research*, VOL. 115, F01009, doi:10.1029/2009JF001444
- 421 Klok, E. J., W. Greuell, and J. Oerlemans (2003), Temporal and spatial variation of
422 the surface albedo of Morteratschgletscher, Switzerland, as derived from 12
423 Landsat images, *J. Glaciol.*, 49, 491–502, doi:10.3189/172756503781830395.
- 424 Mullen, P.C, Warren, S.G., 1988, Theory of the optical properties of lake ice,
425 Volume 93, Issue D7, Pages 8403–8414 DOI: 10.1029/JD093iD07p08403
- 426 Rabatel, A., A. Bermejo, E. Loarte, A. Soruco, J. Gomez, G. Leonardini, C. Vincent, J.-
427 E. Sicart. 2012. Can the snowline be used as an indicator of the equilibrium line and



- 428 mass balance for glaciers in the outer tropics? *Journal of Glaciology*, 58(212), 1027-
429 1036. doi: 10.3189/2012JoG12J027.
- 430 Rabatel, A., B. Francou, A. Soruco, J. Gomez, B. Caceres, J.L. Ceballos, R.
431 Basantes, M. Vuille, J.-E. Sicart, C. Huggel, M. Scheel, Y. Lejeune, Y. Arnaud, M.
432 Collet, T. Condom, G. Consoli, V. Favier, V. Jomelli, R. Galarraga, P. Ginot, L.
433 Maisincho, M. Ménégoz, J. Mendoza, E. Ramirez, P. Ribstein, W. Suarez, M.
434 Villacis, P. Wagnon. 2013. Current state of glaciers in the tropical Andes: a multi-
435 century perspective on glacier evolution and climate change. *The Cryosphere*, 7,
436 81-102. doi:10.5194/tc-7-81-2013.
- 437 Stamnes, K., Tsay, S.-C., Wiscombe, W., and Jayaweera, K.: Numerically stable
438 algorithm for discrete-ordinate-method radiative transfer in multiple scattering and
439 emitting layered media, *Appl. Opt.*, 27, 2502–2509, 1988.
- 440 Sicart, J. E., P. Ribstein, P. Wagnon, and D. Brunstein (2001), Clear sky albedo
441 measurements on a sloping glacier surface. A case study in the Bolivian Andes,
442 *Journal of Geophysical Research*, 106(D23), 31729-31738
- 443 Sicart JE, Hock R, Ribstein P, Litt M and Ramirez E (2011) Analysis of seasonal
444 variations in mass balance and meltwater discharge of the tropical Zongo Glacier
445 by application of a distributed energy balance model. *J. Geophys. Res.*, 116(D13),
446 D13105 (doi: 10.1029/2010JD015105)
- 447 Sicart J.E., Espinoza J.C., Quéno L. and M. Medina. (2016), Radiative properties of
448 clouds over a tropical Bolivian glacier: seasonal variations and relationship with
449 regional atmospheric circulation, *International Journal of Climatology*, Volume 36,
450 Issue 8, 3116–3128 (doi: 10.1002/joc.4540).



- 451 Stroeve, J., A. Nolin, and K. Steffen (1997), Comparison of AVHRRderived and in situ
452 surface albedo over the Greenland Ice Sheet, *Remote Sens. Environ.*, 62, 262–
453 276, doi:10.1016/S0034-4257(97)00107-7.
- 454 Stamnes, K., Tsay, S.-C., Wiscombe, W., and Jayaweera, K., 1988, Numerically
455 stable algorithm for discrete-ordinate-methodradiative transfer in multiple
456 scattering and emitting layered media, *Appl. Opt.*, 27, 2502–2509
- 457 Tachikawa, T., Kaku, M., Iwasaki, A., Gesch, D., Oimoen, M., Zhang, Z., Danielson,
458 J., Krieger, T., Curtis, B., Haase, J., Abrams, M., Crippen, R., Carabajal, C., 2011.
459 ASTER Global Digital Elevation Model Version 2 — Summary of validation results.
460 METI & NASA, (28 pp.).
- 461 van den Broeke, M., D. van As, C. Reijmer, and R. van de Wal, (2004), Assessing
462 and improving the quality of unattended radiation observations in Antarctica, *J.*
463 *Atmos. Oceanic Technol.*, 21, 1417– 1431, doi:10.1175/1520-
464 0426(2004)021<1417:AAITQO>2.0.CO;2.
- 465 Vuille M and Ammann C (1997) Regional snowfall patterns in the high, arid Andes.
466 *Climatic Change*, 36(3–4), 413–423 (doi: 10.1023/A:1005330802974)
- 467 Warren, S.G., 1982, Optical-properties of snow, *Reviews of Geophysics*, 20(1), 67-89